nature communications

Article

https://doi.org/10.1038/s41467-025-59450-6

Sustainable and cost-efficient hydrogen production using platinum clusters at minimal loading

Received: 27 August 2024

Accepted: 23 April 2025

Published online: 09 May 2025

Check for updates

Hongliang Zeng[1,6], Zheng Chen[2,6], Qiu Jiang[1,3] ✉, Qingtian Zhong[1], Yuan Ji[1], Yizhen Chen[4], Jiawei Li[1], Chunxiao Liu[1], Runhao Zhang[1], Jialin Tang[1], Xiaoxia Xiong[1], Zhongyue Zhang[1], Zhaoyang Chen[1], Yizhou Dai[1], Chengbo Li[1], Yinfang Chen[1], Donghao Zhao[1], Xu Li[1], Tingting Zheng[1], Xin Xu[2,5] ✉ & Chuan Xia[1,3] ✉

Proton exchange membrane water electrolysis stands as a promising technology for sustainable hydrogen production, although its viability hinges on minimizing platinum (Pt) usage without sacrificing catalytic efficiency. Central to this challenge is enhancing the intrinsic activity of Pt while ensuring the stability of the catalyst. We herein present a Mo_2TiC_2 MXene-supported Pt nanocluster catalyst (Mo_2TiC_2-Pt_{NC}) that requires a minimal Pt content (36 μg cm^{-2}) to function, yet remains highly active and stable. *Operando* spectroscopy and theoretical simulation provide evidence for anomalous charge transfer from the MXene substrate to Pt_{NC}, thus generating highly efficient electron-rich Pt sites for robust hydrogen evolution. When incorporated into a proton exchange membrane electrolyzer, the catalyst affords more than 8700 h at 200 mA cm^{-2} under ambient temperature with a decay rate of just 2.2 μV h^{-1}. All the performance metrics of the present Mo_2TiC_2-Pt_{NC} catalysts are on par with or even surpass those of current hydrogen evolution electrocatalysts under identical operation conditions, thereby challenging the monopoly of high-loading Pt/C-20% in the current electrolyzer design.

The escalating importance of renewable green hydrogen as an energy vector represents an undeniable facet of the evolving energy landscape[1,2]. A pressing target in the U.S. Department of Energy's (DOE's) Energy Earthshots initiative is to reduce the cost of clean hydrogen to $1 per kilogram in a decade, known as the "111" target[3]. Central to realizing this vision is the application of proton exchange membrane (PEM) water electrolysis technology, noted for its low electrical resistance, high current density, high H_2 purity, and swift device response[4,5]. However, the viability of its commercialization within the hydrogen market is contingent upon the reduction in capital costs. The DOE's 2026 target mandates a total Pt-group metal (PGM) loading below 0.5 mg cm^{-2} for PEM devices[6]. Currently, the Pt content in the cathode alone falls within the range of 0.4–0.6 mg cm^{-2} [7]. This highlights the urgent need to implement low Pt-group metal cathodes, thereby reserving the PGM budget for iridium (Ir) incorporation into the anode (typically more than 5 times the Pt content)[7–12]. Despite progress in developing nonprecious materials for cost efficiency[13–15], Pt remains the material of choice for facilitating the acidic hydrogen evolution reaction (HER) in current commercial PEM water electrolyzers, owing to its unmatched intrinsic activity and stability[16–19].

[1]School of Materials and Energy, University of Electronic Science and Technology of China, Chengdu, P. R. China. [2]Department of Chemistry, Shanghai Key Laboratory of Molecular Catalysis and Innovative Materials, MOE Key Laboratory of Computational Physical Sciences, Fudan University, Shanghai, P. R. China. [3]Yangtze Delta Region Institute (Huzhou), University of Electronic Science and Technology of China, Huzhou, Zhejiang, P. R. China. [4]Department of Chemical Engineering, University of California, Davis, CA, USA. [5]Hefei National Laboratory, Hefei, P. R. China. [6]These authors contributed equally: Hongliang Zeng, Zheng Chen. ✉e-mail: jiangqiu@uestc.edu.cn; xxchem@fudan.edu.cn; chuan.xia@uestc.edu.cn

The HER on metal surfaces such as Pt involves protons from a solution combined with electrons at an electrode. This HER reaction proceeds in two main steps: forming chemisorbed hydrogen atoms on the electrode, followed by H_2 gas evolution. This simple mechanism allows enhancing the HER through two main strategies: maximizing the intrinsic catalytic efficiency and optimizing the exposure of active sites on the catalyst. Nørskov et al. showed the intrinsic HER activity in a "volcano plot" using the binding free energy (ΔG_H) of hydrogen (*H)[20]. They found the highest activity when ΔG_H was near zero, demonstrating that the optimal electrocatalytic sites for the HER should bind *H slightly weaker than metals such as Pd, Rh, or Pt. This could correspond to a more negative chemical state than metallic states[21]. On the other hand, a surface-to-volume ratio can be achieved, for instance, by downsizing bulk catalysts to nanoclusters (NCs) and even to isolated single atoms (SAs). This approach is particularly attractive because it leverages nearly all available platinum atoms, thereby optimizing their effectiveness and enhancing the overall efficiency[22–24]. However, this strategy also exposes more low-coordinate Pt atoms, which have been shown to strongly adsorb *H, consequently reducing the intrinsic activity of Pt. Balancing the metal particle size and maintaining the desired binding energy are critical for developing effective HER catalysts. Moreover, stability is another key factor that must be considered in the utilization of Pt for the HER, as extended electrolysis or a higher current increases the likelihood of Pt agglomeration and thus the degradation of active sites.

Given that the electronic properties of Pt can be fine-tuned by selective bonding with proper supports[25], and that Pt agglomeration can be mitigated through spatial confinement or geometric shielding[26], we envisioned that the intrinsic activity and stability of Pt nanoclusters (Pt_{NC}) could be concurrently modulated by designing supported Pt islands surrounded by functional groups that have high diffusion barriers to isolate these Pt islands. MXenes, first reported by Gogotsi et al. in 2010[27–29], are a class of well-known two-dimensional transition metal carbides or nitrides with layered structures that may serve as an ideal model to validate our hypothesis. In MXenes, early transition metals (M layers) are sandwiched between conductive carbon layers, with abundant surface termination groups, such as O and OH, on the outer M layers[30]. Pursuing this line of inquiry, we synthesized a highly stable and efficient electrocatalyst composed of Pt_{NC} supported on MXene (Mo_2TiC_2-Pt_{NC}) for use in PEM water electrolysis. From our experimental and theoretical evidence, we found anomalous charge transfer from the MXene substrate to Pt_{NC}, which generated highly efficient electron-rich Pt sites for robust hydrogen evolution. The as-synthesized Mo_2TiC_2-Pt_{NC} matches the performance of commercial Pt/C-20%, requiring only an overpotential of 13 ± 3.6 mV to reach 10 mA cm^{-2} while maintaining stability at this current density for more than 280 h. Impressively, our Mo_2TiC_2-Pt_{NC}-based device showcased a robust capability to electrolyze pure water splitting for more than 8700 h at 200 mA cm^{-2} under ambient temperature, when coupled with a commercial oxygen evolution catalyst (IrO_2) in a PEM electrolyzer. Notably, the device delivered a high current density of 1 A cm^{-2} at a low average applied voltage of ~1.65 V and maintained steady operation for over 4800 h under real-world operating conditions (80 °C, 1 bar). Notably, the Pt loading on the cathode in our assembled PEM device is merely 36 μg cm^{-2}, far less than one-tenth of the loading in commercial design. Our Mo_2TiC_2-Pt_{NC} catalyst holds great promise as a viable alternative to commercial Pt/C-20%, representing a prime candidate for satisfying the operational demands of next-generation PEM devices.

Results and discussion

We adopted a straightforward hydrothermal method to synthesize the Mo_2TiC_2-Pt_{NC} catalysts (see details in the Methods and Fig. 1a). The first step involved the synthesis of multi-layered Mo_2TiC_2 (denoted as Mo_2TiC_2-M) via the HF etching method, in which the Al layers were selectively removed from the parent Mo_2TiAlC_2 powder (illustrated in Supplementary Figs. 1–3). Following this, the structure was intercalated with the organic molecule tetrabutylammonium hydroxide (TBAOH), thereby yielding the few-layered Mo_2TiC_2 MXene[29,31]. The process was completed with a thorough washing step to remove any residual TBAOH. The layered structure of Mo_2TiC_2 was evident from the scanning electron microscopy (SEM) image (Fig. 1b). The interlayer spacing of Mo_2TiC_2 was calculated to be 1.8 nm (inset of Fig. 1b) from transmission electron microscopy (TEM), which corresponds to the (002) plane from the X-ray diffraction (XRD) results (Fig. 1f). Finally, by employing Mo_2TiC_2 as a support, we facilitated the deposition of Pt_{NC} via a hydrothermal protocol, incorporating chloroplatinic acid hexahydrate ($H_2PtCl_6{\cdot}6H_2O$) and Mo_2TiC_2 in the process (see Methods for additional details). Quantitative analysis via inductively coupled plasma optical emission spectroscopy (ICP-OES) indicated that the as-prepared Mo_2TiC_2-Pt_{NC} catalyst had a Pt loading of 3.6 ± 0.1 wt% (Supplementary Table 1).

After the hydrothermal reaction, TEM and high-angle annular dark-field scanning TEM (HAADF-STEM) images (Fig. 1c–e) confirmed that the Pt_{NC} were homogeneously sized, with an average diameter of approximately 1.7 nm (Fig. 1d). Furthermore, the results from the high-resolution HAADF-STEM image revealed that the exposed crystal facet of the experimentally prepared Pt_{NC} is the (111) facet (Fig. 1e). The two-dimensional crystal structure of Mo_2TiC_2 was also well maintained (Fig. 1f), suggesting that the incorporation of the Pt precursor into the precursor solution had no discernible effect on the morphology of the MXene structure. For comparison, we also synthesized MXene-supported Pt single atoms (Mo_2TiC_2-Pt_{SA}, 2.7 wt% Pt) and reduced graphene oxide (rGO)-supported Pt_{NC} (rGO-Pt_{NC}, Pt size ~1.5 nm, 4.1 wt% Pt) as controls. The HAADF-STEM images, in conjunction with energy-dispersive spectroscopy (EDS) elemental mapping, unveiled a uniform dispersion of Pt_{SA} or Pt_{NC} across the support structure for the controls (Supplementary Figs. 4–5). Multiple spectra, including XRD and Raman spectroscopy, revealed that both Mo_2TiC_2-Pt_{SA} and Mo_2TiC_2-Pt_{NC} exhibited peak patterns similar to those of Mo_2TiC_2 MXene, indicating the structural stability of the MXene substrate (Supplementary Figs. 6–7). Additionally, Pt_{SA} and Pt_{NC} on the support were distinguished using CO adsorption diffuse reflectance infrared Fourier transform spectroscopy (DRIFTS; see details in Methods). The spectra primarily displayed a strong band at 2105 cm^{-1} for Mo_2TiC_2-Pt_{SA} and 2051 cm^{-1} for Mo_2TiC_2-Pt_{NC}, further substantiating the distinctions in the electronic structure between the two samples (Supplementary Fig. 8)[32].

To reveal the electronic structure of the Pt species within the catalysts, we employed X-ray absorption fine structure (XAFS) and X-ray photoelectron spectroscopy (XPS) analyses. The normalized X-ray absorption near-edge structure (XANES) depicted in Fig. 1g indicated that the white line intensity of the Mo_2TiC_2-Pt_{NC} catalysts was even lower than that of the bulk Pt foil, suggesting a possibly reduced oxidation state. Figure 1h shows the k^3-weighted Fourier transform of the extended X-ray absorption fine structure (EXAFS) at the Pt L_3-edge. We observed a dominant peak at 1.72 Å for Mo_2TiC_2-Pt_{SA}, which corresponded to the Pt-O bond, and no Pt-Pt bonds were observed. This result confirmed that Pt atoms were dispersed as single sites in Mo_2TiC_2-Pt_{SA}, and the evident Pt-O coordination was consistent with previous reports[33,34]. Since the first shell scattering peak in the Pt L_3-edge of Mo_2TiC_2-Pt_{NC} is located within the same distance region as the Pt-Pt scattering peak of Pt foil (R = 1.5–3.2 Å, which corresponds to metal-metal bonding)[35], and the difference in the main peak position is less than 0.1 Å[36,37], distinguishing Pt-Mo and Pt-Pt coordination signals solely through observation of the EXAFS spectrum is challenging. We subsequently performed fitting of the L_3-edge EXAFS of the Mo_2TiC_2-Pt_{NC} and Pt foil. Compared with those of the Pt foil (Supplementary Fig. 9 and Supplementary Table 2), the EXAFS fitting results of Mo_2TiC_2-Pt_{NC} (Supplementary Table 3) reveal a Pt-Mo coordination

https://doi.org/10.1038/s41467-025-59450-6

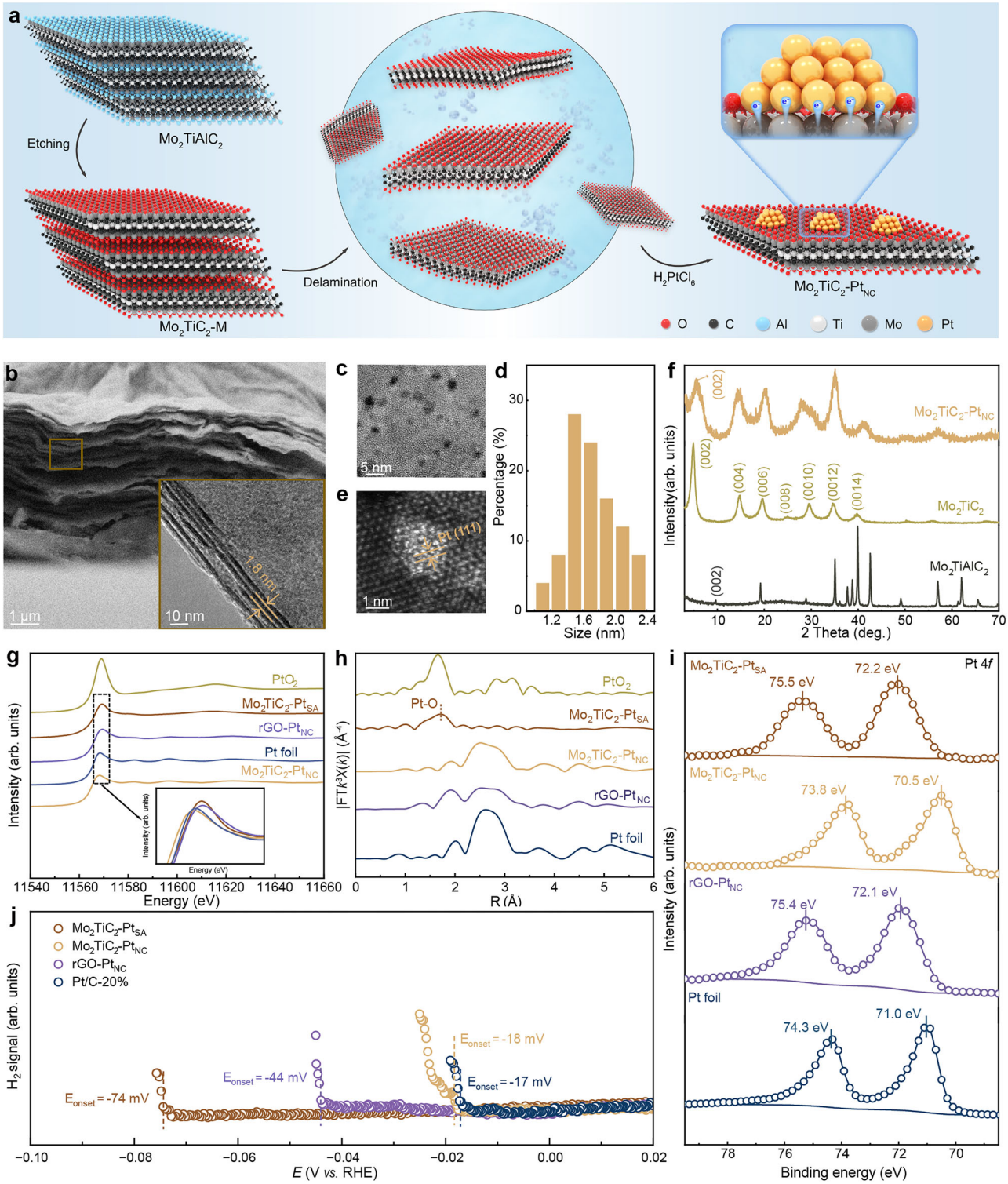

Fig. 1 | Synthesis and structural characterization of the catalyst. a Schematic of the synthesis process of Mo_2TiC_2-Pt_{NC}. **b** SEM and TEM images of few-layer Mo_2TiC_2. **c** TEM image of Mo_2TiC_2-Pt_{NC}. **d** Size distribution of the Pt nanoclusters. **e** HADDF-STEM image of the nanoclusters. **f** XRD spectra of Mo_2TiAlC_2, Mo_2TiC_2, and Mo_2TiC_2-Pt_{NC}. **g** Normalized XANES spectra at the Pt L_3-edge of PtO_2, Mo_2TiC_2-Pt_{SA}, Mo_2TiC_2-Pt_{NC}, rGO-Pt_{NC} and Pt foil. **h** k^3-weighted Fourier transform of EXAFS spectra derived from the EXAFS spectra of PtO_2, Mo_2TiC_2-Pt_{SA}, Mo_2TiC_2-Pt_{NC}, rGO-Pt_{NC}, and Pt foil. *R* is the interatomic distance. **i** High-resolution XPS spectra (Pt 4*f*) of Mo_2TiC_2-Pt_{SA}, Mo_2TiC_2-Pt_{NC}, rGO-Pt_{NC} and Pt foil. (The circles represent raw data, and the lines represent fitting data and base line.) **j** DEMS measurements of Mo_2TiC_2-Pt_{SA}, Mo_2TiC_2-Pt_{NC}, rGO-Pt_{NC} and Pt/C-20%, the onset potentials were determined at points where the signal-to-noise ratio exceeded 5. Source data are provided as a Source Data file.

signal at 2.69 Å, which aligns well with the fitting results of Pt-Mo coordination in other articles[35–37]. Notably, the absence of a Pt-O signal in the Mo_2TiC_2-Pt_{NC} spectrum suggested that the Pt_{NC} on the MXene surface was directly bonded to the MXene lattice rather than to surface oxygen functionalities. Interestingly, the high-resolution Pt 4*f* XPS spectrum revealed that the Mo_2TiC_2-Pt_{NC} catalyst featured a negatively shifted binding energy (70.5 eV and 73.8 eV for the Pt 4*f* 7/2 and 4*f* 5/2 doublets, respectively) in comparison to that of the bulk Pt foil (71 eV and 74.3 eV)[38], in good agreement with the XANES analysis. To validate the robustness of our data, we also calibrated our XPS spectra using Si 2*p* lines as the internal standard. These results were consistent with those obtained using the C 1*s* calibration method (Supplementary Fig. 10). This phenomenon is intriguing, as Pt on most carbon or oxide substrates generally exists in an oxidized or metallic state (Fig. 1i and Supplementary Fig. 11)[39–41]. As expected, Pt in Mo_2TiC_2-Pt_{SA} shows a more positively shifted binding energy than does bulk Pt, which aligns well with previous reports[18,34,42–45]. These findings underscore the size effect on the electronic state of Pt. In contrast, rGO-Pt_{NC} displays more positive binding energy than Pt foil does, highlighting the unique role of the MXene substrate. Taken together, the above results demonstrate that the direct bonding of Pt_{NC} with the MXene lattice results in anomalous electron transfer to Pt atoms, creating an electron-rich Pt surface. Furthermore, the high-resolution Mo 3*d* XPS spectrum shows that Mo_2TiC_2-Pt_{NC} displays more pronounced high-valence Mo signals than Mo_2TiC_2 does (Supplementary Fig. 12), further confirming electron transfer from Mo to Pt_{NC}. This shifts the *d*-band center of Pt downwards from −3.62 (Pt foil) to −3.77 eV (Mo_2TiC_2-Pt_{NC}) (Supplementary Fig. 13), resulting in closer thermal-neutral binding of *H ($\Delta G_H = 0$). Furthermore, we employed *operando* differential electrochemical mass spectrometry (DEMS) to assess the HER capabilities of the different catalysts (Fig. 1j). Impressively, the Mo_2TiC_2-Pt_{NC} catalyst manifested a much lower onset potential than did its counterparts, drawing closer to the commercial benchmark Pt/C-20% catalyst. Simply replacing the MXene substrate with carbon (rGO-Pt_{NC}, with similar Pt dimensions and loading) or decreasing the particle size from Pt_{NC} to Pt_{SA} (Mo_2TiC_2-Pt_{SA}, with similar Pt loading) results in much lower HER activity than Mo_2TiC_2-Pt_{NC} does. This finding implies that the HER activity is closely dependent on the synergistic effect between the Pt metal and MXene substrates. We deduce that the intrinsic activity of the Mo_2TiC_2-Pt_{NC} catalyst is significantly influenced by the unique electron-rich electronic structure of the Pt center due to Pt-MXene interactions.

The HER performances of the different catalysts were then evaluated in detail using a three-electrode setup with Hg/Hg_2SO_4 as the reference electrode and a graphite rod as the counter electrode in H_2-saturated 0.5 M H_2SO_4. Prior to the experimental tests, the reference electrode was meticulously calibrated to a reversible hydrogen electrode (RHE). Linear sweep voltammetry (LSV) curves revealed that the as-prepared Mo_2TiC_2-Pt_{NC} catalyst exhibited effective HER activity with an overpotential of only 13 ± 3.6 mV at 10 mA cm^{-2}, similar to the benchmark Pt/C-20% (14.7 ± 0.6 mV at 10 mA cm^{-2}; Fig. 2a). To further compare the intrinsic HER activity of Mo_2TiC_2-Pt_{NC} with that of the benchmark material, we measured the hydrogen underpotential deposition (H-UPD) features to exclude the contribution of different electrochemical surface area (ECSA, Fig. 2b, c). In a clear demonstration of electrocatalytic performance, a comparison of the LSV curves, normalized using H-UPD, revealed a substantial difference between the two materials. Specifically, Mo_2TiC_2-Pt_{NC} showed an intrinsic performance of 1.55 ± 0.4 mA $cm^{-2}{}_{ECSA}$ (the specific value in Fig. 2c is 1.99 mA $cm^{-2}{}_{ECSA}$) which was 4.8 times greater than that of the benchmark Pt/C-20% of 0.32 ± 0.04 mA $cm^{-2}{}_{ECSA}$, measured at an overpotential of 31 mV. Additionally, Mo_2TiC_2-Pt_{NC} demonstrated a Tafel slope of 24 mV dec^{-1}, a value that was comparable to the Tafel slope observed for Pt/C-20% (Fig. 2d). This similarity in the Tafel slopes suggested that the kinetic rate-step process of Mo_2TiC_2-Pt_{NC} was consistent with that of Pt/C-20%, following the same mechanism referred to as the Tafel step. To further describe the elementary reaction in the HER process on Mo_2TiC_2-Pt_{NC}, we conducted *operando* electrochemical impedance spectroscopy (EIS) experiments (Fig. 2e and Supplementary Figs. 15, 16). Specifically, we observed that Mo_2TiC_2-Pt_{NC} exhibited only one phase angle, indicative of the same Volmer-Tafel kinetic process that characterizes commercial Pt/C-20%. This finding stands in stark contrast to the two-phase angles typically observed in the Volmer-Heyrovsky kinetic process[46,47].

We further quantitatively analyzed HER activity in terms of mass activity and turnover frequency (TOF, normalized to the active site density) (Fig. 2f). Specifically, at an overpotential of 60 mV, the mass activity of Mo_2TiC_2-Pt_{NC} was estimated to be 3.3 ± 1.31 A mg^{-1}, which was substantially greater than that of Pt/C-20% (0.72 ± 0.19 A mg^{-1}) and Mo_2TiC_2-Pt_{SA} (0.35 ± 0.07 A mg^{-1}). At the same overpotential, a significant difference in the TOF was observed. Specifically, the TOF of Mo_2TiC_2-Pt_{NC} was found to be 9.45 ± 3.71 s^{-1}. This value not only outperforms the benchmark Pt/C-20% (1.82 ± 0.48 s^{-1}) but also surpasses Mo_2TiC_2-Pt_{SA} (0.36 ± 0.07 s^{-1}). Notably, the TOF represents a lower bound for the true activity of Mo_2TiC_2-Pt_{NC} because a subset of the Pt atoms remains inaccessible within the bulk, coupled with the constraints posed by mass transport limitations[48].

In addition to the above performance, maintaining robust electrolytic stability is the key. We further evaluated the stability of Mo_2TiC_2-Pt_{NC} and found that it maintained a hydrogen Faradaic efficiency (FE) close to 100% across different current densities (Supplementary Fig. 17). Additionally, stable hydrogen production was achieved through electrolysis at 10 mA cm^{-2} for over 280 h (Fig. 2g). Accelerated stability tests revealed virtually no decay after 10,000 cycles (Supplementary Fig. 18). Structural characterization *via* XRD, SEM, XPS, TEM and XAFS (XANES and EXAFS) further demonstrated that the structure was almost unchanged after the durability test (Supplementary Figs. 19, 20). Consequently, the aforementioned attributes of Mo_2TiC_2-Pt_{NC}, including its low overpotential, reduced Tafel slope, and slow decay rate, were found to surpass those of most previously reported Pt-based catalysts (Supplementary Fig. 21 and Supplementary Table 5).

To explore the impact of the substrate on the loaded Pt_{NC}, the HER mechanism was further analyzed utilizing the equivalent circuit depicted in Supplementary Fig. 22. This approach allowed for a detailed examination of the underlying electrochemical processes, providing insights into the specific interactions and dynamics that govern the reaction kinetics. The intermediate coverage on the catalyst surface can be represented by two parallel components (C_φ and R_2, which represent the hydrogen adsorption pseudo-capacitance and resistance, respectively) in the equivalent circuit[49]. As illustrated in Supplementary Figs. 23, 24, the adsorption charges of hydrogen on the surfaces of Mo_2TiC_2-Pt_{NC} and rGO-Pt_{NC} were obtained through EIS fitting. Notably, Mo_2TiC_2-Pt_{NC} exhibited more hydrogen adsorption charges (750 μC) than did rGO-Pt_{NC} (624 μC). This result indicates a much greater surface intermediate coverage on Mo_2TiC_2-Pt_{NC}, despite its quite similar Pt dimensions and content to those of rGO-Pt_{NC}. Such a difference highlights the critical role of electron enrichment on the Pt surface of Mo_2TiC_2-Pt_{NC}.

Additionally, we compared the in situ attenuated total reflection surface-enhanced infrared absorption spectroscopy (ATR-SEIRAS) of Mo_2TiC_2-Pt_{SA}, rGO-Pt_{NC}, and Mo_2TiC_2-Pt_{NC} under different applied potentials (0.1 to −0.1 V) (Supplementary Fig. 25). Among these catalysts, Mo_2TiC_2-Pt_{NC} exhibited the highest $\upsilon_{O\text{-}H}$ wavenumber, indicating the weakest degree of hydrogen bonding in its interfacial water[50,51]. This characteristic facilitates more efficient intermediate transport, thereby increasing the reaction kinetics. We further investigated the effect of the substrate by comparing the activity and stability of Mo_2TiC_2-Pt_{NC} and rGO-Pt_{NC}. A comparison was made under identical conditions, with both substrates having similar particle sizes of Pt_{NC}

https://doi.org/10.1038/s41467-025-59450-6

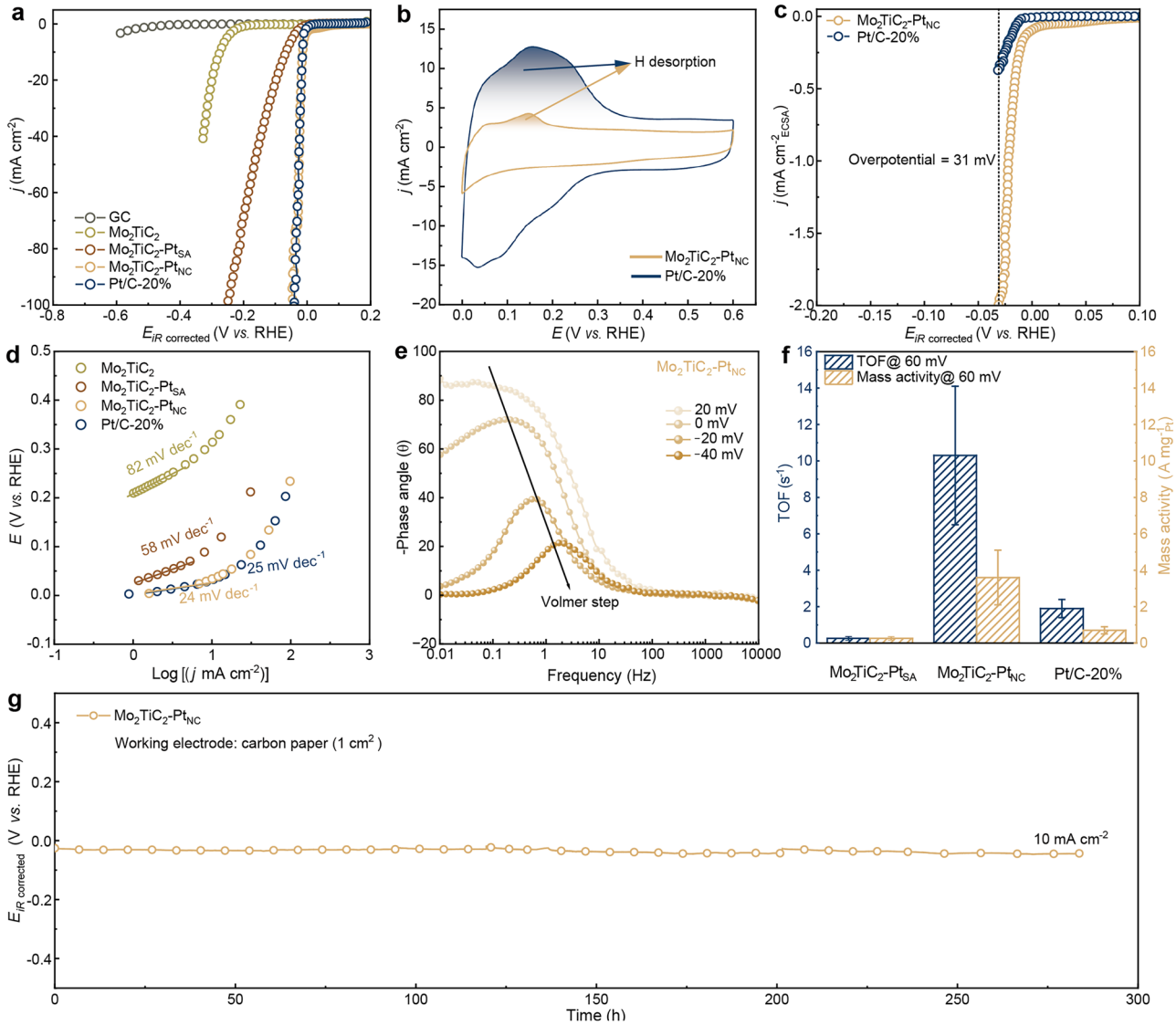

Fig. 2 | Electrocatalytic performance of the catalysts. a The *iR*-corrected polarization curves of glass carbon (GC), Mo_2TiC_2 ($R = 3.378\ \Omega$), Mo_2TiC_2-Pt_{SA} ($R = 2.18\ \Omega$), Mo_2TiC_2-Pt_{NC} ($R = 1.763\ \Omega$) and Pt/C-20% ($R = 1.433\ \Omega$) acquired using a graphite rod as the counter electrode in 0.5 M H_2SO_4 (GCE electrode surface area: 1.13 cm^2, catalyst loading: 1 mg cm^{-2}, rotation rate: 1600 rpm, pH value of the electrolyte (H_2SO_4): 0.43 ± 0.02, and all measurements were conducted at ambient temperature. All error bars in Fig. 2 represent the standard deviation. All potentials are 100% *iR* compensated, and all non-*iR* corrected data and corresponding resistance values for three independent samples are shown in Supplementary Fig. 14 and Supplementary Table 4, respectively). **b** H-UPD region of Mo_2TiC_2-Pt_{NC} and Pt/C-20% obtained from the cyclic voltammetry curve (Scan rate: 50 mV s^{-1}). **c** ECSA-normalized (H-UPD) HER polarization curves of Mo_2TiC_2-Pt_{NC} and Pt/C-20% in 0.5 M H_2SO_4. **d** Tafel slopes of Mo_2TiC_2, Mo_2TiC_2-Pt_{SA} Mo_2TiC_2-Pt_{NC} and Pt/C-20%. **e** *Operando* EIS tests of Mo_2TiC_2-Pt_{NC}. **f** Calculated TOF and mass activity values at an overpotential of 60 mV in 0.5 M H_2SO_4. **g** Stability test of Mo_2TiC_2-Pt_{NC} through chronopotentiometry at a current density of 10 mA cm^{-2} in 0.5 M H_2SO_4. Source data are provided as a Source Data file.

and Pt loading. As shown in Supplementary Figs. 26, 27, the performance of rGO-Pt_{NC} was found to be inferior, and its stability at a current density of 10 mA cm^{-2} clearly decreased over a period of 70 h. These results collectively affirm that the high structural stability of Mo_2TiC_2-Pt_{NC} can be attributed to the unique interaction between the Pt and MXene supports.

Density functional theory (DFT) calculations were performed to elucidate the origin of the high stability and high HER activity of Mo_2TiC_2-Pt_{NC}, where unique metal-support interactions play a pivotal role, as indicated by comparisons with controls. Considering the computational consumption and experimental size of Pt_{NC}, a Pt_{31} model was chosen for simulation, which mostly exposes the (111) facet, as revealed by the previous HAADF-STEM image in Fig. 1e. Although the supported model involving metal binding to surface oxygen (Fig. 3a) is a common alternative, a model in which Pt_{31} binds to Mo (Fig. 3b) was employed here due to the absence of a Pt-O signal for Mo_2TiC_2-Pt_{NC} from experimental observations (Fig. 1h). DFT calculations revealed that the two different models resulted in opposite charge transfer directions (Fig. 3a, b). In contrast to the commonly observed charge transfer from the metal to the support, the latter model showed a significant charge transfer reversal from the support to the metal, which is consistent with the XPS observations (Fig. 1i). Thus, both the experimental and theoretical findings corroborate the hypothesis that Pt_{NC} binds to outer Mo sites, which aligns with the fact that TiC_2 layers are sandwiched between Mo layers in Mo_2TiC_2[30]. Moreover, this model showed a much stronger metal-support interaction (−2.81 eV per interacting atom; Fig. 3b) than that of the model in which Pt_{31} bound to the surface oxygen (−0.79 eV per interacting atom; Fig. 3a), which even surpassed the binding strength between Pt_{31} and the Pt (111) surface (−2.11 eV per interacting atom; Fig. 3c). This result

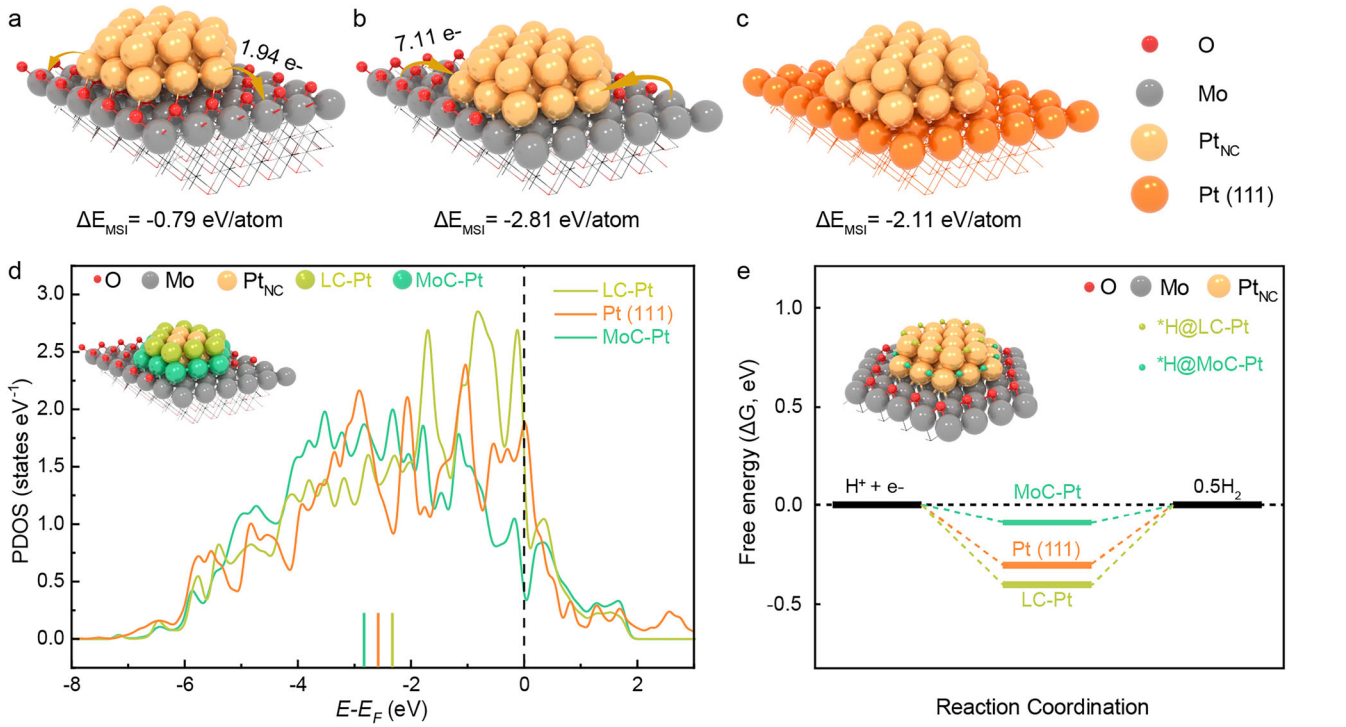

Fig. 3 | DFT calculations for elucidating the stability and activity. The models for Pt_{NC} are supported on the (**a**) surface oxygen of Mo_2TiC_2, (**b**) Mo of Mo_2TiC_2, and (**c**) Pt (111) surface. ΔE_{MSI}: strength of the metal-support interaction. **d** The *d*-electron structure of on-surface Pt atoms on the Pt (111) surface and Mo_2TiC_2-Pt_{NC}, including LC-Pt and MoC-Pt, respectively. **e** Free energy diagram of hydrogen evolution at zero potential and pH 0 for the Pt (111) surface and Mo_2TiC_2-Pt_{NC}, including LC-Pt and MoC-Pt. Atomic coordinate dataset is provided as Supplementary Data 1, other source data are provided as a Source Data file.

indicates that Mo_2TiC_2 with oxygen functional groups can act as a bifunctional heteroenergetic support. The Mo-block anchors and secures the Pt_{NC} in place, resulting in anomalous charge transfer, while the O-block isolates the Pt_{NC}, preventing particle migration and coalescence and inhibiting Ostwald ripening[26]. Therefore, the unique structure of Mo_2TiC_2-Pt_{NC} enables the achievement of high stability for nanoscale Pt_{NC}, which is consistent with experimental observations (Fig. 2g).

As indicated by the charge transfer observed in both the experimental (Fig. 1i) and theoretical (Fig. 3b) results, the unique metal-support interaction also significantly tunes the electronic structure of Pt_{NC} and thus the HER activity. Figure 3d shows the *d*-electron structures of the surface Pt atoms on Mo_2TiC_2-Pt_{NC}, which included low-coordinate Pt (LC-Pt) and Mo-coordinate Pt (MoC-Pt). Compared with that of the surface Pt on the Pt (111) slab, the *d*-band center of LC-Pt is upshifted as expected, whereas that of MoC-Pt is downshifted. This is consistent with the downshift in the *d*-band center of Mo_2TiC_2-Pt_{NC} observed via XPS (−3.77 eV) compared with that of the Pt foil (−3.62 eV; Supplementary Fig. 13). A downshift of the *d*-band center weakens the binding of *H and moves it toward the optimal value, which is subsequently evidenced by the calculated adsorption-free energy of *H (Fig. 3e). The weakened *H binding increases the intrinsic HER activity by accelerating the Tafel steps, which has been identified as the rate-determining step for both Pt/C and Mo_2TiC_2-Pt_{NC} (Fig. 2e and Supplementary Fig. 15). Conversely, for the model with Pt_{NC} supported on graphene instead of Mo_2TiC_2-Pt_{NC} (Supplementary Fig. 28), Pt atoms at the interface were found to bind *H as strongly as LC-Pt. Therefore, the metal-support interaction of Mo_2TiC_2-Pt_{NC} enables us to overcome the disadvantage of decreasing the Pt size, where increasing the exposure of LC-Pt would strengthen *H binding and decrease the intrinsic HER activity.

Finally, to assess the capacity of our Mo_2TiC_2-Pt_{NC} to electrolyze water in an industrial setting, we utilized PEM devices assembled with a membrane electrode assembly (MEA) specifically for the electrolysis of pure water (Fig. 4a). A commercial PEM device (Pt/C-20%||IrO_2) with a loading of 500 μg cm^{-2} Pt was included for comparison. Although we lack the specific expertise and equipment to fabricate industrial-grade, high-quality membrane electrodes with minimal ionic resistance between the cathode and anode, this does not compromise the validity of the performance comparison. We sandwiched the Nafion 117 membrane between Mo_2TiC_2-Pt_{NC} and commercial IrO_2 for PEM water electrolysis, with a loading of 36 μg cm^{-2} Pt (1 mg cm^{-2} catalyst, see Supplementary Fig. 29 for Pt load optimization). We assessed stable electrolytic hydrogen production at room temperature. Although the Pt loading in our case is substantially lower than that in commercial designs, the performance of our device, when directly compared, aligns with the levels observed in contemporary commercial designs, operating under an equivalent bias voltage (Fig. 4b). Moreover, our Mo_2TiC_2-Pt_{NC} based cell was able to electrolyze hydrogen for more than 8700 h at 200 mA cm^{-2}. This was achieved with an overpotential of ~1.97 V and a degradation rate of only 2.2 μV h^{-1} (Fig. 4c), which matches the DOE's 2026 target (2.3 μV h^{-1}).

In addition, the stability of such devices was better than that of recently reported precious metal catalysts (Supplementary Table 6). We further conducted electrolysis experiments on the Mo_2TiC_2-Pt_{NC} based cell under industrial working conditions (1 A cm^{-2}, 1 bar at 80 °C). By constantly regulating the parameters during the assembly process of the device, the impedance between the cathode and anode in our device can be reduced to 15–20 mΩ cm^{-2}; as a result, the device can run stably for hydrogen production for 4800 h at 1 A cm^{-2} (Fig. 4c). According to the calculation from DOE's suggestion (see details in Note 1), note that the clean electricity price of $0.03 per kWh, as proposed by the DOE, was employed in our calculation[52,53], only US$ 1.327 was required to produce 1 kg H_2 with this device, well below the DOE goal of 2026 (<US$ 2 kg^{-1} H_2). Compared with other membrane electrode assembly water electrolyzers (MEAWEs) with cathodic PGM

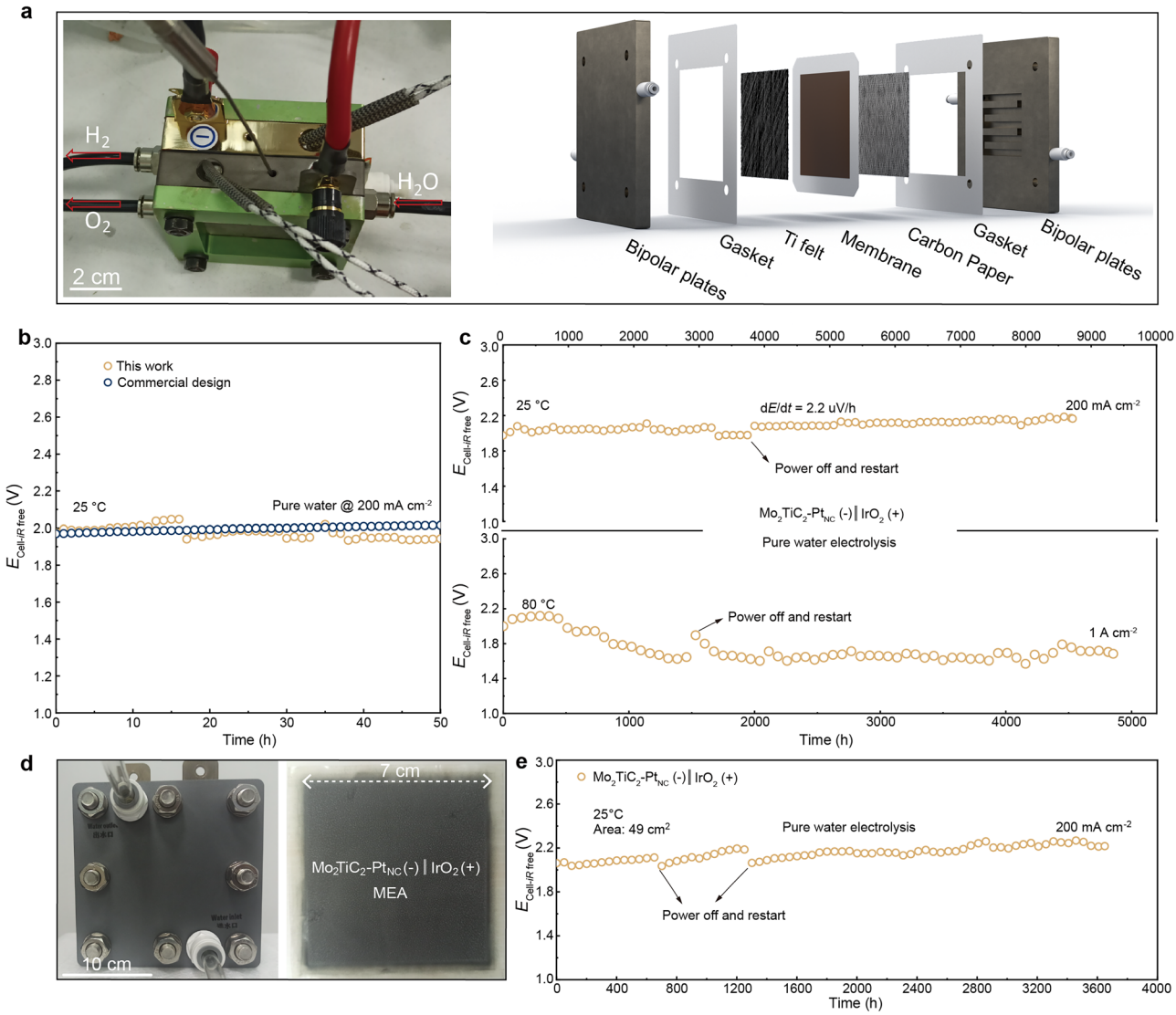

Fig. 4 | Performance of PEM water electrolyzers (PEMWE) devices. a Photograph and schematic of the PEMWE device. **b** Chronopotentiometry test of a 4 cm^2 Pt/C-20%||IrO_2 PEMWE device at 200 mA cm^{-2} (25 °C, ambient pressure), compared with a Mo_2TiC_2-Pt_{NC} device. **c** Long-term electrolytic test of PEMs assembled with Mo_2TiC_2-Pt_{NC} at 200 mA cm^{-2} and 1 A cm^{-2} using commercial IrO_2 as the anode catalyst, at 25 °C and 80 °C, respectively. Discontinuities in voltage arise from the unexpected power off. **d** Photograph of the 49 cm^2 device and MEA membrane together with the Mo_2TiC_2-Pt_{NC} cathode and IrO_2 anode layers. **e** Long-term stability of the 49 cm^2 device at ambient pressure. All the performance tests of the aforementioned PEMWE devices were conducted without *iR* correction. Source data are provided as a Source Data file.

catalysts, the observed superiority of Mo_2TiC_2-Pt_{NC} as a cathode catalyst underscores its potential for industrial applications (Table 1). This potential is further emphasized by our ability to achieve gram-scale synthesis of the catalyst (Supplementary Fig. 30). To demonstrate the availability of our catalyst in mass hydrogen generation, we also conducted a constant electrolytic hydrogen production test on an extended electrode area (49 cm^2) of the Mo_2TiC_2-Pt_{NC} based cell, which outputs over 4.09-liter pure hydrogen per hour, and the stability exceeded 3600 h (Fig. 4d, e). The findings reported here could contribute to future developments in large-area membrane electrode assembly and reactor implementation, highlighting its potential for industrial applications.

In conclusion, to alleviate the usage of Pt-group precious metals in acidic water electrolysis, we developed a catalyst (Mo_2TiC_2-Pt_{NC}), featuring a low Pt mass loading on MXenes. The interaction between Pt and the support induces electron enrichment on the Pt surface, enabling thermo-neutral hydrogen adsorption. Consequently, the catalyst achieved electrolytic performance and stability on par with commercial Pt/C-20%. Notably, our Mo_2TiC_2-Pt_{NC} catalyst demonstrated a robust capacity for hydrogen production at 200 mA cm^{-2} over 8700 h in a PEM device, and even under industrial conditions (1 A cm^{-2}, 1 bar at 80 °C), it maintained stability for more than 4800 hours. Therefore, we identified a catalyst with the potential to replace commercial Pt/C-20% for water electrolysis in industrial-scale PEM devices. This advancement could help reduce catalyst costs and support the broader adoption of PEM reactors and grid implementations.

Methods

Materials synthesis

Chemicals. Ethanol, Nafion 117 perfluorinated resin solution (5 wt%), chloroplatinic acid hexahydrate ($H_2PtCl_6{\cdot}6H_2O$) and tetrabutylammonium hydroxide ($C_{16}H_{37}NO$) were purchased from Macklin. Graphene oxide (GO) was purchased from Suzhou Tanfeng Graphene Technology Co., Ltd. Pt/C (nominally 20 wt% on carbon black) was purchased from Johnson Matthey. All reagents were used without further purification. All aqueous solutions were prepared with

Table 1 | Performance metrics of different MEAWEs with cathodic Pt group metal (PGM) catalysts

	Cathodic PGM loading (μg cm^{-2})	Current density (mA cm^{-2})	Stability (h)	Degradation rate (μV h^{-1})
This work	36	200 1000	8700+ 4800+	2.2[a] /
PEMWEs[67–69]	40–500	100–1000	48–500	83.33–200
AEMWEs[70–72]	14–278	270–1000	20–2000	40–1600
Neutral MEAWEs[50,73]	>47	100–150	40	700–3500

[a]Owing to an unforeseen power interruption at approximately 3840 h, the degradation rate was determined based on the initial continuous operation of 3840 h.

Millipore water (resistivity of 18.2 MΩ cm). The detailed parameters are provided in Supplementary Table 7.

Synthesis of multilayer Mo_2TiC_2 MXene. Mo_2TiAlC_2 MAX-phase powder (2.0 g) was slowly added to an HF (40%, 20 ml) solution in a Teflon beaker under continuous stirring for 120 h at 55 °C. The product was centrifuged and washed several times in argon-saturated water until the pH approached 6 or 7. The suspension was freeze-dried at −59 °C for 48 h to obtain dry multilayer Mo_2TiC_2 powders.

Synthesis of fewer-layer Mo_2TiC_2 MXene. Multilayer Mo_2TiC_2 MXene (1.0 g) was added to 20 ml of organic solvent (54–56 wt% TBAOH ($(C_4H_9)_4NOH$)) and stirred at 50 °C for 24 h. The resulting mixture was centrifuged and washed three times in deionized water to separate the MXene from TBAOH. After the upper layer was emptied, 100 ml of deionized water was added, and the mixture was sonicated for 1 h in an ice bath, followed by centrifugation for 1 h at 3500 rpm (~1370 × *g*) to obtain fewer-layer MXenes with uniform dispersion.

Synthesis of Mo_2TiC_2-Pt_{NC}. The sample was prepared using a standard hydrothermal technique. Specifically, 50 mg of few-layered Mo_2TiC_2 MXene was uniformly dispersed in 25 ml of deionized water with 7.65 mg of $H_2PtCl_6{\cdot}6H_2O$. This mixture was then subjected to ultrasonic agitation to achieve a homogenous solution. The mixture was transferred to a 50 ml Teflon-lined autoclave and reacted at 180 °C for 0.5 h. After naturally cooling to room temperature, the products were washed and centrifuged three times with deionized water to obtain the Mo_2TiC_2-Pt_{NC} catalysts.

Synthesis of Mo_2TiC_2-Pt_{SA} and rGO-Pt_{NC}. The synthesis of Mo_2TiC_2-Pt_{SA} was performed via a hydrothermal method similar to that used for Mo_2TiC_2-Pt_{NC}. First, 5.5 mg of $[Pt(NH_3)_4](NO_3)_2$ was added to a 50 ml solution of 50 mg of Mo_2TiC_2 and heated at 140 °C for 1 h to obtain Mo_2TiC_2-Pt_{SA} after centrifugation and washing. The preparation of rGO-Pt_{NC} was achieved by a simple impregnation method. Specifically, 7.65 mg of $H_2PtCl_6{\cdot}6H_2O$ was added to 25 ml of aqueous solution containing 50 mg of GO to form a uniform dispersion. The mixture was further freeze-dried for 48 h at −59 °C, Following this, it was transferred to a tube furnace and reacted at 450 °C under a 5% H_2/Ar atmosphere for 2 h, resulting in the rGO-Pt_{NC} product.

Characterizations

Scanning electron microscopy (SEM) was performed on a Gemini-SEM300 electron microscope. Powder X-ray diffraction (PXRD) was performed using Cu *K*α radiation (λ = 1.54178 Å) by a Philips X'Pert Pro Super diffractometer. Raman spectra were obtained using a LabRAM HR laser Raman analyzer with an excitation wavelength of 785 nm. Transmission electron microscopy (TEM) was performed on a Tecnai G2 F20 S-Twin TMP transmission electron microscope with an acceleration voltage of 200 kV. X-ray photoelectron spectroscopy (XPS) was performed on an Axis Supra photoelectron spectrometer using an exciting source of Al *K*α radiation (1486.6 eV), and the binding energy of the C 1*s* peak (284.8 eV) was selected as the actual reference. HADDF−STEM and EDS elemental mapping were performed on a Themis Z field-emission transmission electron microscope at an acceleration voltage of 200 kV. The Pt concentrations of all the samples were measured using inductively coupled plasma optical emission spectroscopy (ICP-OES, Avio 500). In situ diffuse reflectance Fourier transform infrared spectroscopy (DRIFTS) experiments were conducted on a Thermo Scientific Nicolet iS50 FTIR spectrometer with ZnSe as the prismatic window at room temperature. XAS measurements at the Pt L_3-edge of the samples were carried out on the BL14W1 beamline of the Shanghai Synchrotron Radiation Facility, operated in fluorescent mode on all samples. XAFS data processing and fitting were carried out with Demeter software.

CO DRIFTS. The adsorption behavior of CO on the Mo_2TiC_2-Pt_{SA} and Mo_2TiC_2-Pt_{NC} catalysts was studied by diffuse reflectance Fourier transform infrared spectroscopy (DRIFTS). DRIFTS spectra were collected on a Thermo Scientific Nicolet iS50 FTIR spectrometer at a resolution of 8 cm^{-1}. The infrared cell was first partially filled with inert KBr powder and filled with catalysts on the KBr holder. For fresh catalysts, pretreatment at 100 °C and Ar for 30 min was performed to remove impurities (H_2O) that may be adsorbed on the surface. Then, the background spectrum was recorded after the reaction cell was cooled to 25 °C. Then, CO adsorption was conducted with a mixture of 10% CO/Ar (15 ml min^{-1}) and Ar (30 ml min^{-1}) for 20 min. Furthermore, gas-phase CO in the reaction cell was removed by Ar purging at a flow rate of 30 ml min^{-1}, after which the desorption spectrum of the catalyst-adsorbed CO was recorded. CO adsorption experiments were carried out at 25 °C.

In situ DEMS tests. For the in situ DEMS test, 2 mg of each catalyst was mixed with 5 wt% Nafion (20 μl) in 980 μl of ethanol and then sonicated for 20 min to form a homogeneous solution. A 0.01 ml of ink was drop-cast onto a glassy carbon (diameter of 0.3 cm) working electrode. The electrodes were dried at room temperature for at least 30 min. In situ differential electrochemical mass spectrometry (DEMS) was performed using a custom capillary electrochemical mass spectrometer single cell. A capillary was inserted into the in situ cell, close to the side above the working electrode. The gaseous product was introduced into a DEMS sensor (PrismaPro). Linear sweep voltammetry was performed on the cathode at a scan rate of 1 mV s^{-1}. A photograph of the in situ DEMS setup is provided in Supplementary Fig. 31.

In situ ATR-SEIRAS test. 4 mg of each catalyst was mixed with 40 μl of Nafion (5 wt%) and 960 μl of ethanol and then sonicated for 20 min to form a homogeneous solution. A 0.238 ml of ink was dropped on a gold-plated silicon crystal (usable area of 0.95 cm^2) with a typical catalyst loading (~1 mg cm^{-2}). For constant potential testing, the potential was varied from 0.1 to −0.1 V versus RHE, and the infrared spectral data were recorded. A photograph of the in situ ATR-SEIRAS setup is provided in Supplementary Fig. 32.

All the detailed configurations of the in situ electrochemical cells used are provided in Supplementary Table 8.

Electrochemical measurements

Calibration of the reference electrode and conversion to RHE scale. A mercury-mercurous sulfate reference electrode (Hg/Hg_2SO_4) was used in all the measurements. The calibration of the reference electrode was performed in the standard three-electrode configuration. Polished platinum foil was used as the working and counter electrode, and Hg/Hg_2SO_4 was used as the reference electrode. The electrolyte was purged and saturated with high-purity H_2 before measurement

and was kept flowing during the calibration process. Cyclic voltammetry (CV) was then run at a scan rate of 1 mV s^{-1}, and the average potential at which the current crossed zero was taken as the thermodynamic potential for the hydrogen electrode reactions. In our experiment, in 0.5 M H_2SO_4, the zero current point was calculated to be 0.697 V.

Therefore, $E(\mathrm{RHE}) = E(\mathrm{Hg/Hg_2SO_4}) + 0.697\ \mathrm{V}$

Measurement of the electrode material. All the electrochemical performance tests were performed at room temperature by a Bio-Logic VMP3 electrochemical workstation with a typical three-electrode system. A glass carbon electrode with a diameter of 1.2 cm was selected as the working electrode, $Hg/HgSO_4$ was used as the reference electrode, and a graphite rod was used as the counter electrode. An H-type cell was used as the electrolytic cell (a Nafion membrane was used to separate the anode and cathode chambers). The $Hg/HgSO_4$ electrode was calibrated in a H_2-saturated 0.5 M H_2SO_4 electrolyte. The preparation, storage and pH values of the electrolyte (0.5 M H_2SO_4, pH value: 0.43 ± 0.02) are provided in Supplementary Fig. 33 and Note 2.

To prepare the working electrode ink, 4 mg of each catalyst was mixed with 40 µl of Nafion (5 wt%) and 960 µl of ethanol and then sonicated for 20 min to form a homogeneous solution. A 0.283 ml of ink was dropped on glass carbon (area of 1.13 cm^2) with a typical catalyst loading (~1 mg cm^{-2}). Additionally, the cathode chamber was separated from the anode chamber (counter electrode: graphite rod) by a Nafion 117 membrane (the activation process of the Nafion membrane is provided in Note 3). For the performance test, the cathode chamber was placed on a magnetic stirring table (~1600 rpm) to facilitate the rapid desorption of H_2 gas bubbles. Linear sweep voltammetry was carried out in 0.5 M H_2SO_4 at a scan rate of 5 mV s^{-1}, deaerated with Ar. Cyclic voltammetry was performed in the potential window from 0.15 V to −1.5 V (versus RHE) for 10000 cycles (scan rate of 50 mV s^{-1}). Electrochemical resistance measurements were performed at the OCV with the frequency range from 0.01 Hz to 10^6 Hz (*operando* EIS tests were performed at potentials ranging from 0.02 V to −0.05 V (versus RHE), and the resistance values were calculated from the high frequency intercepts with the X-axis on the Nyquist plot. The Tafel test was performed by chronoamperometry[54], which is more accurate than the Tafel value obtained from the polarization curve. Cyclic voltammetry and potential-time stability tests were conducted with a catalyst loading of ~1 mg cm^{-2} on 1 cm^2 carbon paper.

Additionally, the constant potential test was conducted using the "Chronoamperometry" function in BioLogic VMP3, whereas the constant current test was performed using the "Chronopotentiometry" function in BioLogic VMP3. Data acquisition and processing were carried out using the corresponding software, "EC-Lab", via a USB serial connection.

The FE of Mo_2TiC_2-Pt_{NC} was calculated using the following Eq. (1).

$$FE = \frac{n \cdot F \cdot n(H_2)}{i \cdot t} \cdot 100\% \tag{1}$$

where n represents the number of electron transfer involved in the HER, F denotes the Faraday constant (96,485 C mol^{-1}), $n_{(H_2)}$ denotes the number of moles of H_2 detected by gas chromatography (GC) during HER electrolysis (using GC to detect the volume of H_2, applying the ideal gas equation to convert to $n_{(H_2)}$), i represents the applied current, and t represents the reaction time of HER electrocatalysis.

The ECSA of Pt was estimated by measuring the H-UPD characteristics. CV measurements were performed in a three-electrode system (with an Ar-saturated 0.5 M H_2SO_4 solution) collected from 0 to 0.6 V versus RHE at a scan rate of 50 mV s^{-1}. Calculated from the region of hydrogen desorption charge (~0–0.5 V versus RHE) on the CV curves. Calculate ECSA using the following Eq. (2).

$$ECSA_{\mathrm{Pt}} = \frac{S_Q(A \cdot V)/v(V\,s^{-1})}{210(\mu c\ cm_{Pt}^{-2})} \tag{2}$$

where S_Q is the integral area of the hydrogen desorption charge region in the CV curve. v is the scan rate and 210 µC cm_{Pt}^{-2} for a monolayer H-UPD at Pt.

The TOF values were calculated based on the number of surface active Pt atoms in each catalyst (the TOF value of Mo_2TiC_2-Pt_{SA} was calculated from the mass of Pt) on the electrode according the following Eq. (3).

$$TOF = \frac{1}{2} \cdot \frac{i(A)/F(C\ mol^{-1})}{S_Q(A\,V)/v(V\,s^{-1})F(C\ mol^{-1})} \tag{3}$$

where i represents the current recorded from the LSV curves.

The mass activity was determined using the following Eq. (4).

$$Mass\ activity = \frac{i(A)}{m_{Pt}(mg)} \tag{4}$$

where m_{Pt} is the mass of Pt in each catalyst on the electrode.

Performance of the membrane electrode devices. To prepare the membrane electrode device, the anodic catalyst IrO_2 was selected for the oxygen evolution reaction (OER), and Pt/C (20 wt%, Johnson Matthey) or Mo_2TiC_2-Pt_{NC} was used as the cathode HER catalyst. For commercial design, a slurry composed of Pt/C, Nafion (5 wt%) and ethanol was evenly sprayed on both sides of the proton exchange membrane (Nafion 117), with mass loading of 1 mg cm^{-2} Ir and 0.5 mg cm^{-2} Pt. The PEM device with Mo_2TiC_2-Pt_{NC} catalyst is prepared in the same procedure and the mass loadings of IrO_2 and Mo_2TiC_2-Pt_{NC} were controlled to be 1 mg cm^{-2} Ir and 36 µg cm^{-2} Pt, respectively. After drying, the membrane electrode was hot-pressed (100 °C) at a pressure of 2 MPa for 10 min. Titanium felt and carbon paper were used as the anode and cathode gas diffusion layers, and a peristaltic pump (2.5 ml min^{-1}) was used for pure water circulation to the anodic side. A Fumasep FS-990-PK membrane was used to fabricate the 49 cm^2 PEM device following the same preparation procedures described previously. All the cell tests were performed at ambient pressure, and none of the measured cell voltages were *iR* compensated. The details of the catalyst loading calculation and the geometric dimensions of the electrodes are provided in Note 4.

In a PEM water electrolyzer test, a DC current power supply (DCPS0614, 30 V/20 A) was employed as a constant potentiostat. Stability tests were performed in constant current mode, with data collected and processed using the "DC Power Supply" software connected via a USB serial port.

Computational methods

The Vienna ab initio simulation package (VASP)[55–57] was used for all density functional theory (DFT) calculations. In these simulations, the valence electrons were defined as follows: the 1*s* electron in H, the 2*s* and 2*p* electrons in C and O, the 3*d* and 4*s* electrons in Ti, the 4*d*, 4*p*, and 5*s* electrons Mo, and the 5*d* and 6*s* electrons in Pt[58]. A plane-wave basis set was employed with a kinetic energy cutoff of 450 eV. Core electrons were treated using the projector augmented-wave (PAW) method[59]. Monkhorst–Pack meshes[60] of 2 × 2 × 1 sampling in the Brillouin zone were employed for the slab models.

For pristine Mo_2TiC_2-O_2, a 6 × 6 supercell with one layered structure was chosen. For pristine graphene, an 8 × 8 supercell was chosen. For pristine Pt(111), a 6 × 6 supercell with four layers was chosen. Except for the bottom two layers of the Pt(111)-based cases, all the atoms were relaxed. Convergence of the geometry optimization

was assumed when the force on each atom was less than 0.02 eV Å^{-1}[61]. The Perdew-Burke-Ernzerhof (PBE) functional, within the generalized gradient approximation (GGA), was employed for all calculations[62]. Dispersion interactions were accounted for using the DFT + D3 method with Becke-Jonson (BJ) damping[63,64].

The free energy of the adsorbed state was calculated using Eq. (5):

$$\Delta G_H = \Delta E_H + \Delta E_{ZPE} - T\Delta S \quad (5)$$

where ΔE_H is the adsorption energy of hydrogen, ΔE_{ZPE} is the difference corresponding to the zero point energy between the adsorbed state and the gas phase, and $T\Delta S$ is the term corresponding to the entropy correction of hydron adsorption. As reported in previous work, a value of ΔE_{ZPE} -$T\Delta S$ of 0.24 eV is employed here[65].

In the free energy diagram of the HER, the Gibbs free energy change (ΔG) of the proton-coupled electron transfer (PCET) step was calculated using the computational hydrogen electrode (CHE) model[20,66], which defines the chemical potential of the proton-electron pair as half of the chemical potential of hydrogen.

Note 1 | Techno-economic analysis

Considering that the cost of noble metals in the cathode accounts for a high proportion of the total MEA cost (0.4–0.6 mg cm^{-2}), cost accounting of the cathodic noble metals is necessary. The price of the noble metal (Pt) was obtained from the *Johnson Matthey Price Charts*.

1) The cathodic noble metal content of our PEM electrolyzer is 0.036 mg cm^{-2}, which is much lower than the reported cathode platinum load (0.4–0.6 mg cm^{-2}). Our cathodic platinum metal cost is only \$0.01181 cm^{-2}.

2) The energy efficiency of a PEM electrolyzer can be calculated by the following equation:

$$\text{Energy efficiency} = \frac{1.23\,V}{U_{cell}} = \frac{1.23\,V}{1.65V} \times 100\% = 74.5\% \quad (6)$$

where 1.23 V represents the theoretical energy of the products and U_{cell} is the cell voltage (V) required to deliver a current density of 1 A cm^{-2}.

3) The energy consumption of a PEM electrolyzer is calculated by the following equation:

$$\text{Energy consumption} = \frac{U_{cell} I_{cell} t}{m_{H_2}} = \frac{1.65V \times 4A \times 4000h}{596.98\,g} = 44.22\,\text{kWh kg}^{-1}\text{H2} \quad (7)$$

where I_{cell} is the current delivered (A), t is the operation time (h), and m_{H_2} is the mass of hydrogen produced in a t duration, which can be calculated by Faraday's laws of electrolysis:

$$m_{H_2} = \frac{I_{cell} \times t}{z \times F} \times M_{H_2} = \frac{4A \times 4000 \times 3600s}{2 \times 96485.3C/mol} \times 2g/mol = 596.98g \quad (8)$$

z in Eq. (8) is the number of electrons transferred to produce one hydrogen molecule, M_{H_2} is the relative molecular mass (2 g mol^{-1}).

The energy efficiency and energy consumption of our PEM electrolyzer are superior to those of the targets (69% and 48 kWh kg^{-1}H_2 for 2026) set by the US Department of Energy.

4) Cost of H_2 per kilogram of hydrogen:

Cost (H_2/kg) = energy consumption × electricity price

=44.22 kWh/kg H_2 × \$0.03/kWh

=\$1.327/kg H_2

Our H_2 production cost is much lower than the target (\$2/kg H_2 for 2026) set by the US Department of Energy.

Note 2|Preparation and storage of the electrolyte

The 0.5 M H_2SO_4 electrolyte was freshly prepared before each use using the following procedure. First, 486.4 ml of deionized water was measured and transferred into a 500 ml volumetric flask. Next, 13.6 ml of concentrated H_2SO_4 (98%) was carefully measured using a 20 ml pipette and slowly added to the volumetric flask while gently swirling the solution to ensure thorough mixing. The solution was then allowed to cool to room temperature. Once cooled, deionized water was gradually added to the volumetric flask until the solution's meniscus reached the calibration mark. The solution was then sealed and stored in a cool, dry place for use.

Note 3|Activation process of the Nafion 117 membrane

The Nafion 117 membrane, with a thickness of 183 μm, was used when fabricating the three-electrode and MEA device and underwent an activation process prior to use: the membrane was first treated in a 5% hydrogen peroxide solution at 80 °C for 1 h to remove organic impurities. It was then rinsed by soaking in deionized water for 30 minutes to eliminate any residual peroxide. The membrane was subsequently treated in a 5% dilute sulfuric acid solution at 80 °C for 1 h to increase its proton conductivity, followed by a final rinse in deionized water for 30 min to remove any remaining acid.

Note 4|Details of the catalyst loading calculation and geometric dimensions of the electrodes

In a three-electrode test, the catalyst slurry concentration (c) was 4 mg ml^{-1}, and the glassy carbon electrode area (s) was 1.13 cm^2 (diameter of 1.2 cm). A catalyst drop volume (v) of 0.283 ml was applied, resulting in a catalyst loading (m) on the electrode calculated as

$$m = v \cdot c/s \approx 1\,\text{mg cm}^{-2}$$

In situ DEMS tests, for a catalyst slurry concentration of 2 mg ml^{-1}, a glassy carbon electrode area of 0.0707 cm^2 (diameter of 0.3 cm), and a catalyst drop volume of 0.01 ml, the catalyst loading (excessive loading of the catalyst on such an electrode can cause catalyst detachment, leading to unreliable experimental results) was calculated as

$$m = v \cdot c/s \approx 0.283\,\text{mg cm}^{-2}$$

In situ ATR-SEIRAS test, for a catalyst slurry concentration of 4 mg ml^{-1}, a usable gold-plated silicon crystal area of 0.95 cm^2 (diameter of 1.1 cm), and a catalyst drop volume of 0.238 ml, the catalyst loading was calculated as

$$m = v \cdot c/s \approx 1\,\text{mg cm}^{-2}$$

Data availability

All data were available in the main text or the supplementary materials. Source data are provided with this paper.

References

1. van Renssen, S. The hydrogen solution? *Nat. Clim. Chang.* **10**, 799–801 (2020).
2. Dresselhaus, M. S. & Thomas, I. L. Alternative energy technologies. *Nature* **414**, 332–337 (2001).
3. Hydrogen Shot|Department of Energy. https://www.energy.gov/eere/fuelcells/hydrogen-shot.
4. Terlouw, T., Bauer, C., McKenna, R. & Mazzotti, M. Large-scale hydrogen production *via* water electrolysis: a techno-economic and environmental assessment. *Energy Environ. Sci.* **15**, 3583–3602 (2022).

5. King, L. A. et al. A non-precious metal hydrogen catalyst in a commercial polymer electrolyte membrane electrolyser. *Nat. Nanotechnol.* **14**, 1071–1074 (2019).
6. Technical Targets for Proton Exchange Membrane Electrolysis | Department of Energy. https://www.energy.gov/eere/fuelcells/technical-targets-proton-exchange-membrane-electrolysis.
7. Yu, H. & Yi, B. Hydrogen for energy storage and hydrogen production from electrolysis. *Chin. J. Eng. Sci.* **20**, 58 (2018).
8. Minke, C., Suermann, M., Bensmann, B. & Hanke-Rauschenbach, R. Is iridium demand a potential bottleneck in the realization of large-scale PEM water electrolysis? *Int J. Hydrog. Energy* **46**, 23581–23590 (2021).
9. An, L. et al. Recent development of oxygen evolution electrocatalysts in acidic environment. *Adv. Mater.* **33**, 2006328 (2021).
10. Chen, Z. et al. Advances in oxygen evolution electrocatalysts for proton exchange membrane water electrolyzers. *Adv. Energy Mater.* **12**, 2103670 (2022).
11. Liang, Q. & Li, D. Activating localized lattice oxygen for durable acidic water oxidation. *Chem. Catal.* **1**, 506–508 (2021).
12. Tymoczko, J., Calle-Vallejo, F., Schuhmann, W. & Bandarenka, A. S. Making the hydrogen evolution reaction in polymer electrolyte membrane electrolysers even faster. *Nat. Commun.* **7**, 10990 (2016).
13. Pan, S. et al. Efficient and stable noble-metal-free catalyst for acidic water oxidation. *Nat. Commun.* **13**, 2294 (2022).
14. Staszak-Jirkovský, J. et al. Design of active and stable Co–Mo–Sx chalcogels as pH-universal catalysts for the hydrogen evolution reaction. *Nat. Mater.* **15**, 197–203 (2016).
15. Zhang, X.-L. et al. Efficient acidic hydrogen evolution in proton exchange membrane electrolyzers over a sulfur-doped marcasite-type electrocatalyst. *Sci. Adv.* **9**, eadh2885 (2023).
16. Yang, H. et al. Metastable-phase platinum oxide for clarifying the Pt–O active site for the hydrogen evolution reaction. *Energy Environ. Sci.* **16**, 574–583 (2023).
17. Subbaraman, R. et al. Enhancing hydrogen evolution activity in water splitting by tailoring Li^+-$Ni(OH)_2$-Pt interfaces. *Science* **334**, 1256–1260 (2011).
18. Shi, Y. et al. Electronic metal–support interaction modulates single-atom platinum catalysis for hydrogen evolution reaction. *Nat. Commun.* **12**, 3021 (2021).
19. Hansen, J. N. et al. Is there anything better than Pt for HER? *ACS Energy Lett.* **6**, 1175–1180 (2021).
20. Nørskov, J. K. et al. Trends in the exchange current for hydrogen evolution. *J. Electrochem Soc.* **152**, J23 (2005).
21. Yan, Q.-Q. et al. Reversing the charge transfer between platinum and sulfur-doped carbon support for electrocatalytic hydrogen evolution. *Nat. Commun.* **10**, 4977 (2019).
22. Wang, A., Li, J. & Zhang, T. Heterogeneous single-atom catalysis. *Nat. Rev. Chem.* **2**, 65–81 (2018).
23. Liu, L. & Corma, A. Metal catalysts for heterogeneous catalysis: from single atoms to nanoclusters and nanoparticles. *Chem. Rev.* **118**, 4981–5079 (2018).
24. Chen, Y. et al. Single-atom catalysts: synthetic strategies and electrochemical applications. *Joule* **2**, 1242–1264 (2018).
25. Rong, H., Ji, S., Zhang, J., Wang, D. & Li, Y. Synthetic strategies of supported atomic clusters for heterogeneous catalysis. *Nat. Commun.* **11**, 5884 (2020).
26. Hu, S. & Li, W.-X. Sabatier principle of metal-support interaction for design of ultrastable metal nanocatalysts. *Science* **374**, 1360–1365 (2021).
27. Naguib, M., Mochalin, V. N., Barsoum, M. W. & Gogotsi, Y. 25th anniversary article: mxenes: a new family of two-dimensional materials. *Adv. Mater.* **26**, 992–1005 (2014).
28. Gogotsi, Y. & Anasori, B. The rise of MXenes. *ACS Nano* **13**, 8491–8494 (2019).
29. Naguib, M. et al. Two-dimensional nanocrystals produced by exfoliation of Ti3AlC2. *Adv. Mater.* **23**, 4248–4253 (2011).
30. Anasori, B. et al. Two-dimensional, ordered, double transition metals carbides (MXenes). *ACS Nano* **9**, 9507–9516 (2015).
31. Naguib, M., Unocic, R. R., Armstrong, B. L. & Nanda, J. Large-scale delamination of multi-layers transition metal carbides and carbonitrides "MXenes". *Dalton Trans.* **44**, 9353–9358 (2015).
32. Bazin, P. et al. FT-IR study of CO adsorption on Pt/CeO_2: characterisation and structural rearrangement of small Pt particles. *Phys. Chem. Chem. Phys.* **7**, 187–194 (2005).
33. Zhao, D. et al. MXene (Ti_3C_2) vacancy-confined single-atom catalyst for efficient functionalization of CO_2. *J. Am. Chem. Soc.* **141**, 4086–4093 (2019).
34. Zhang, J. et al. Single platinum atoms immobilized on an MXene as an efficient catalyst for the hydrogen evolution reaction. *Nat. Catal.* **1**, 985–992 (2018).
35. Li, Z. et al. Direct methane activation by atomically thin platinum nanolayers on two-dimensional metal carbides. *Nat. Catal.* **4**, 882–891 (2021).
36. Mao, J. et al. Design of ultrathin Pt-Mo-Ni nanowire catalysts for ethanol electrooxidation. *Sci Adv* **3** (2017).
37. Zhang, X. et al. A stable low-temperature H_2-production catalyst by crowding Pt on α-MoC. *Nature* **589**, 396–401 (2021).
38. Moulder, J. F., Stickle, W. F., Sobol, P. E., Bomben, K. D. & Chastain, J. *Handbook of X-Ray Photoelectron Spectroscopy A Reference Book of Standard Spectra for Identification and Interpretation of XPS Data* (Physical Electronics Division, Perkin-Elmer Corporation, 1979).
39. Zhao, Y. et al. Modulating Pt-O-Pt atomic clusters with isolated cobalt atoms for enhanced hydrogen evolution catalysis. *Nat. Commun.* **13**, 2430 (2022).
40. Xiong, M. et al. In situ tuning of electronic structure of catalysts using controllable hydrogen spillover for enhanced selectivity. *Nat. Commun.* **11**, 4773 (2020).
41. Wang, X. et al. Atomic-precision Pt6 nanoclusters for enhanced hydrogen electro-oxidation. *Nat. Commun.* **13**, 1596 (2022).
42. Zhou, K. L. et al. Platinum single-atom catalyst coupled with transition metal/metal oxide heterostructure for accelerating alkaline hydrogen evolution reaction. *Nat. Commun.* **12**, 3783 (2021).
43. Cheng, N. et al. Platinum single-atom and cluster catalysis of the hydrogen evolution reaction. *Nat. Commun.* **7**, 13638 (2016).
44. Liu, D. et al. Atomically dispersed platinum supported on curved carbon supports for efficient electrocatalytic hydrogen evolution. *Nat. Energy* **4**, 512–518 (2019).
45. Fang, S. et al. Uncovering near-free platinum single-atom dynamics during electrochemical hydrogen evolution reaction. *Nat. Commun.* **11**, 1029 (2020).
46. Yan, P. et al. One stone five birds" plasma activation strategy synergistic with Ru single atoms doping boosting the hydrogen evolution performance of metal hydroxide. *Adv. Funct. Mater.* **33**, 2301343 (2023).
47. Chen, W. et al. Deciphering the alternating synergy between interlayer Pt single-atom and NiFe layered double hydroxide for overall water splitting. *Energy Environ. Sci.* **14**, 6428 (2021).
48. Zalitis, C. M., Kramer, D., Sharman, J., Wright, E. & Kucernak, A. R. Pt nano-particle performance for PEFC reactions at low catalyst loading and high reactant mass transport. *ECS Trans.* **58**, 39–47 (2013).
49. Li, J. et al. Ethylene-glycol ligand environment facilitates highly efficient hydrogen evolution of Pt/CoP through proton concentration and hydrogen spillover. *Energy Environ. Sci.* **12**, 2298–2304 (2019).
50. Sun, K. et al. Interfacial water engineering boosts neutral water reduction. *Nat. Commun.* **13**, 6260 (2022).

51. Li, P. et al. Hydrogen bond network connectivity in the electric double layer dominates the kinetic pH effect in hydrogen electrocatalysis on Pt. *Nat. Catal.* **5**, 900–911 (2022).
52. Hao, S. et al. Torsion strained iridium oxide for efficient acidic water oxidation in proton exchange membrane electrolyzers. *Nat. Nanotechnol.* **16**, 1371–1377 (2021).
53. Shi, Z. et al. Customized reaction route for ruthenium oxide towards stabilized water oxidation in high-performance PEM electrolyzers. *Nat. Commun.* **14**, 843 (2023).
54. Anantharaj, S. et al. The pitfalls of using potentiodynamic polarization curves for tafel analysis in electrocatalytic water splitting. *ACS Energy Lett.* **6**, 1607–1611 (2021).
55. Kresse, G. & Hafner, J. Ab initio molecular dynamics for open-shell transition metals. *Phys. Rev. B* **48**, 13115–13118 (1993).
56. Kresse, G. & Furthmüller, J. Efficiency of ab initio total energy calculations for metals and semiconductors using a plane-wave basis set. *Comput. Mater. Sci.* **6**, 15–50 (1996).
57. Kresse, G. & Furthmüller, J. Efficient iterative schemes for ab initio total-energy calculations using a plane-wave basis set. *Phys. Rev. B.* **54**, 11169–11186 (1996).
58. Niu, W. et al. Pb-rich Cu grain boundary sites for selective CO-to-n-propanol electroconversion. *Nat. Commun.* **14**, 4882 (2023).
59. Blochl, P. E. Projector augmented-wave method. *Phys. Rev. B* **50**, 17953–17979 (1994).
60. Monkhorst, H. J. & Pack, J. D. Special points for Brillouin-zone integrations. *Phys. Rev. B* **13**, 5188–5192 (1976).
61. Sun, S. et al. Potassium-promoted limestone for preferential direct hydrogenation of carbonates in integrated CO_2 capture and utilization. *JACS Au* **4**, 72–79 (2024).
62. Perdew, J. P., Burke, K. & Ernzerhof, M. Generalized gradient approximation made simple. *Phys. Rev. Lett.* **77**, 3865–3868 (1996).
63. Grimme, S., Antony, J., Ehrlich, S. & Krieg, H. A consistent and accurate ab initio parametrization of density functional dispersion correction (DFT-D) for the 94 elements H-Pu. *J. Chem. Phys.* **132**, 154104 (2010).
64. Grimme, S., Ehrlich, S. & Goerigk, L. Effect of the damping function in dispersion corrected density functional theory. *J. Comput. Chem.* **32**, 1456–1465 (2011).
65. Chen, Z. et al. Accurate descriptions of molecule-surface interactions in electrocatalytic CO_2 reduction on the copper surfaces. *Nat. Commun.* **14**, 936 (2023).
66. Nørskov, J. K. et al. Origin of the overpotential for oxygen reduction at a fuel-cell cathode. *J. Phys. Chem. B* **108**, 17886–17892 (2004).
67. Dong, S. et al. Overall design of anode with gradient ordered structure with low iridium loading for proton exchange membrane water electrolysis. *Nano Lett.* **22**, 9434–9440 (2022).
68. Liu, W. et al. Single-layer platinum cluster catalyst for efficient hydrogen electro-production. *Adv. Funct. Mater.* **33**, 2212752 (2023).
69. Shi, Z. et al. Phase-dependent growth of Pt on MoS_2 for highly efficient H_2 evolution. *Nature* **621**, 300–305 (2023).
70. Gao, L. et al. Engineering a local potassium cation concentrated microenvironment toward the ampere-level current density hydrogen evolution reaction. *Energy Environ. Sci.* **16**, 285–294 (2023).
71. Zhao, J. et al. Activating Ru-O-Co interaction on the *a*-$Co(OH)_2$ @Ru interface for accelerating the volmer step of alkaline hydrogen evolution. *Small Methods* **7**, 2201362 (2023).
72. Zhang, T. et al. Pinpointing the axial ligand effect on platinum single-atom-catalyst towards efficient alkaline hydrogen evolution reaction. *Nat. Commun.* **13**, 6875 (2022).
73. Zheng, X. et al. Tailoring a local acid-like microenvironment for efficient neutral hydrogen evolution. *Nat. Commun.* **14**, 4209 (2023).

Acknowledgements

The authors acknowledge the National Key Research and Development Program of China (2024YFB4105700, 2022YFA1504402), National Natural Science Foundation of China (22405035, 52171201, 22233002, 22103014), Natural Science Foundation of Sichuan Province (2025NSFJQ0017, 24NSFSC5779), the Innovation Program for Quantum Science and Technology (2021ZD0303305), the China Postdoctoral Science Foundation funded project (2022M710601), and the Huzhou Science and Technology Bureau (2023GZ02). We thank beamline BL14W1 of the Shanghai Synchrotron Radiation Facility for providing the facilities.

Author contributions

The project was conceptualized by C.X. and supervised by C.X., X.X. and Q.J. H.Z. prepared the catalysts. H.Z., Q.Z., J.L. and C.L. performed the catalytic tests. H.Z., Y.J., R.Z., Z.Z., Z.X., Y.C. and D.Z. performed the catalyst characterizations. X.Xiong, Zhao.C., Y.D. and C.L. performed the XAFS measurements. Yi.C., J.T., T.Z. and X.L. helped in the analysis of the data. Z.C. and X.X. performed the DFT calculations. C.X., Q.J., X.X., Z.C. and H.Z. wrote the paper with input from all the authors. All the authors discussed the results and commented on the manuscript.

Competing interests

A China provisional patent application (202310633252.7) based on the technology described in this work was filed in July 2023 by C.X., H.Z. and Q.J. at the University of Electronic Science and Technology of China. The other authors declare no competing interests.

Additional information

Supplementary information The online version contains supplementary material available at https://doi.org/10.1038/s41467-025-59450-6.

Correspondence and requests for materials should be addressed to Qiu Jiang, Xin Xu or Chuan Xia.

Peer review information *Nature Communications* thanks Min-Rui Gao, Xiong Peng and the other anonymous reviewer(s) for their contribution to the peer review of this work. A peer review file is available.